bioRxiv preprint doi: https://doi.org/10.1101/2022.01.06.475200; this version posted January 6, 2022. The copyright holder for this preprint (which was not certified by peer review) is the author/funder, who has granted bioRxiv a license to display the preprint in perpetuity. It is made available under aCC-BY-NC-ND 4.0 International license.

# Resonant waves drive long-range correlations in fMRI signals

Joana Cabral[1,2†], Francisca F. Fernandes[2], Noam Shemesh[2†]

[1] Life and Health Sciences Research Institute, School of Medicine, University of Minho, Braga, Portugal

[2] Champalimaud Research, Champalimaud Centre for the Unknown, Lisbon, Portugal

**One Sentence Summary:** (max 125 char)

Brain functional connectivity driven by spatially defined oscillatory modes

Word Count: ~4000 (including Figure captions)

[†]Correspondence:

Dr. Noam Shemesh
Champalimaud Research, Champalimaud Centre for the Unknown
Av. Brasilia 1400-038, Lisbon, Portugal.
E-mail: noam.shemesh@neuro.fchampalimaud.org
Phone number: +351 210 480 000 ext. #4467.

Dr. Joana Cabral
Life and Health Sciences Research Institute, University of Minho
Campus de Gualtar, 4710-057 Braga, Portugal
E-mail: joanacabral@med.uminho.pt
Phone number: +351 919 289 649

bioRxiv preprint doi: https://doi.org/10.1101/2022.01.06.475200; this version posted January 6, 2022. The copyright holder for this preprint (which was not certified by peer review) is the author/funder, who has granted bioRxiv a license to display the preprint in perpetuity. It is made available under aCC-BY-NC-ND 4.0 International license.

## Abstract

The fundamental principles driving spontaneous long-range correlations between distant brain areas - known as intrinsic functional connectivity - remain unclear. To investigate this, we develop an ultrafast functional Magnetic Resonance Imaging (fMRI) approach with unprecedented temporal resolution (38 milliseconds) in the rat brain. We detect a repertoire of principal components exhibiting standing wave properties, i.e., with phase relationships varying gradually across space and oscillating in time, driving in- and anti-phase synchronization across distinct cortical and subcortical structures. The spatial configuration, stability and peak frequency of these standing waves is found to depend on the sedation/anaesthesia state, with medetomidine sedation revealing the most stable (i.e., less damped) standing waves, resonating at frequencies extending up to 0.25 Hz. Our findings show that the complex activity patterns observed in resting-state fMRI signals result from the superposition of standing waves, supporting the hypothesis that intrinsic functional connectivity is inherently associated to resonance phenomena.

bioRxiv preprint doi: https://doi.org/10.1101/2022.01.06.475200; this version posted January 6, 2022. The copyright holder for this preprint (which was not certified by peer review) is the author/funder, who has granted bioRxiv a license to display the preprint in perpetuity. It is made available under aCC-BY-NC-ND 4.0 International license.

## Introduction

Correlated activity across spatially segregated brain subsystems in the absence of stimulus - typically described as resting-state or intrinsic functional connectivity - appears disrupted in numerous neuropsychiatric disorders and is therefore assumed to play a key role in brain function (*1-4*). However, the fundamental principles driving long-range correlations detected with functional Magnetic Resonance Imaging (fMRI) remain unclear (*5-8*).

Distinct 'intrinsic connectivity networks' defined as subsets of brain areas exhibiting correlated activity have been consistently identified across mammals (*9-13*). Dynamically, these intrinsic networks have been shown to emerge transiently and recurrently over time (*14, 15*). More recently, these structured fluctuations in fMRI signals have been shown to be tightly related to systemic physiological processes (*5, 16-18*). Still, current experimental results provide little insight into the principles driving their spontaneous self-organization.

At the local level, ultra-slow oscillations in fMRI signals have been shown to be coupled with electrophysiological and electroencephalographic (EEG) signals, pointing to a relationship with the underlying neural activity (*18-22*). However, how these spontaneous sub-hertz oscillations organize at the macroscopic scale and their relationship to long-range functional connectivity remains completely unknown, mainly due to insufficient spatiotemporal resolution of contemporary neuroimaging techniques.

Increased sensitivity can be achieved with the use of cryogenic coils, which significantly increase the signal to noise ratio by attenuating thermal noise, allowing to further investigate the oscillatory nature of fMRI-based functional connectivity with high field magnets in rats. Interestingly, fMRI signals in rats are known to be strongly affected by the sedation/anaesthesia state (*23, 24*). In particular, sedation with low doses of medetomidine has been shown to reveal consistent resting-state networks analogous to the ones identified in humans (*25-27*), but also to drive high amplitude oscillations in fMRI signals at frequencies

bioRxiv preprint doi: https://doi.org/10.1101/2022.01.06.475200; this version posted January 6, 2022. The copyright holder for this preprint (which was not certified by peer review) is the author/funder, who has granted bioRxiv a license to display the preprint in perpetuity. It is made available under aCC-BY-NC-ND 4.0 International license.

extending beyond 0.1 Hz (*24, 28*). The addition of isoflurane at low concentrations suppresses these oscillations while maintaining the activity in the typical range of resting-state frequencies, such that the combination medetomidine/isoflurane (MED/ISO) is currently the state-of-the-art protocol to approximate 'awake' brain activity in rats (*29*). Still, the origin and role of the oscillations detected in fMRI signals across sedation/anaesthesia protocols remain unclear.

To address this caveat, we harness an ultrafast fMRI approach with unprecedented temporal resolution of 38 milliseconds in a single slice of the rat brain, achieving high signal to noise ratio via a high 9.4 Tesla magnetic field and a cryogenic coil. This approach exposes unreported features of rat brain activity, providing insights into the fundamental principles driving long-range functional connectivity in the brain.

## Results

Results from a typical seed-based correlation analysis are shown in **Figure 1** to confirm the detection of long-range correlations in fMRI signals in the range of frequencies typically considered in resting-state studies (cf. Supplementary Figure S1 for the corresponding brain atlas). In panel c, we plot the fMRI signals in 3 different seeds together with their contralateral voxels. As expected, the correlation is not constant but fluctuates between periods of strong positive correlation and periods of weak or even negative correlation. To show that these effects are not merely scanner-driven, the same figure for a rat scanned postmortem is reported in Supplementary Figure S2.

bioRxiv preprint doi: https://doi.org/10.1101/2022.01.06.475200; this version posted January 6, 2022. The copyright holder for this preprint (which was not certified by peer review) is the author/funder, who has granted bioRxiv a license to display the preprint in perpetuity. It is made available under aCC-BY-NC-ND 4.0 International license.

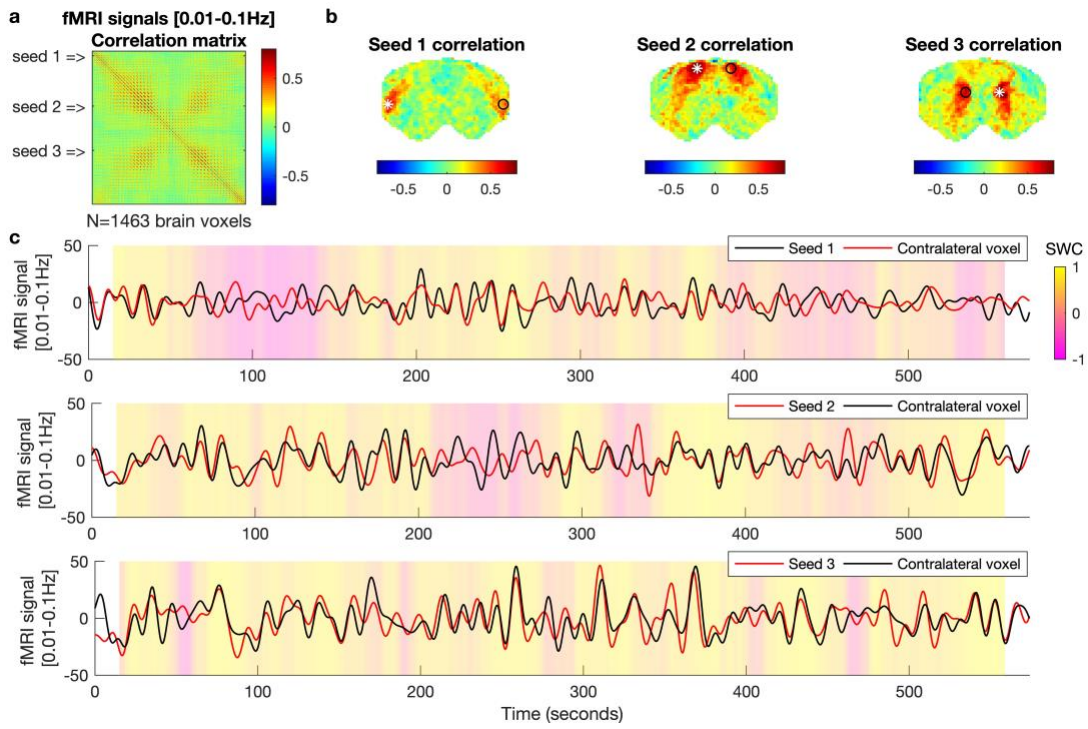


***Figure 1 – Typical resting-state functional connectivity analysis in band-pass filtered fMRI signals. (a)*** *Correlation matrix of the fMRI signals in all voxels within the brain mask, bandpass filtered in a range typically considered in resting-state studies, i.e., 0.01-0.1Hz (no nuisance regressor nor spatial smoothing applied). Each line/column in the matrix corresponds to the correlation map of each voxel.* ***(b)*** *Seed-based correlation maps are represented for 3 different seeds (white asterisks), where each voxel is colored according to its degree of correlation with the seed. A voxel contralateral to each seed is represented by a black circle. All colorbars are truncated between -0.8 and 0.8.* ***(c)*** *Filtered fMRI signals recorded in each seed (red) and corresponding contralateral voxel (black). Colored shades represent the sliding window correlation (SWC) using a 30-second window, showing that correlation is not constant but fluctuates in time. The same figure obtained from a postmortem scan is reported in SI figure S2.*

To investigate the hypothesis that correlations are inherently associated with oscillatory phenomena, we turn to evaluate the range of frequencies with power above postmortem baseline across three different sedation/anaesthesia protocols: under medetomidine only (which we term *sedation*), after the addition of isoflurane at 1% concentration (*light anaesthesia*), and after increasing isoflurane concentration to 3% (*deep anaesthesia*) (see Methods for details). Applying a space-frequency analysis on the 36 ultrafast fMRI scans (each 10 minute long at 26.3 Hz sampling rate), the 3 different conditions are compared in terms of power at different frequency bands across brain voxels (**Figure 2**). Power at frequencies up to 0.30 Hz – extending well beyond the range typically considered in resting-state studies - is detected in the brains of sedated and lightly anaesthetized rats significantly above deep anaesthesia levels (**Figure 2**b, p-values in Figure S3). Notably, the

bioRxiv preprint doi: https://doi.org/10.1101/2022.01.06.475200; this version posted January 6, 2022. The copyright holder for this preprint (which was not certified by peer review) is the author/funder, who has granted bioRxiv a license to display the preprint in perpetuity. It is made available under aCC-BY-NC-ND 4.0 International license.

most powerful oscillations are detected in sedated animals between 0.20 and 0.25 Hz, peaking in power (i.e., squared amplitude) within well-defined cortical boundaries, whereas the striatum (subcortical) appears to resonate mostly between 0.1 and 0.15Hz (**Figure 2**). The addition of isoflurane at 1% is found to specifically affect the power of cortical oscillations between 0.15-0.25Hz, whereas isoflurane at 3% significantly decreases the power in the broad frequency range between 0.05 and 0.3Hz (**Figure 2**b and Fig. S4). Above 0.40 Hz, only signatures associated to heartbeat and breathing frequencies are detected (Supplementary section I, Fig. S5 and Table S1).

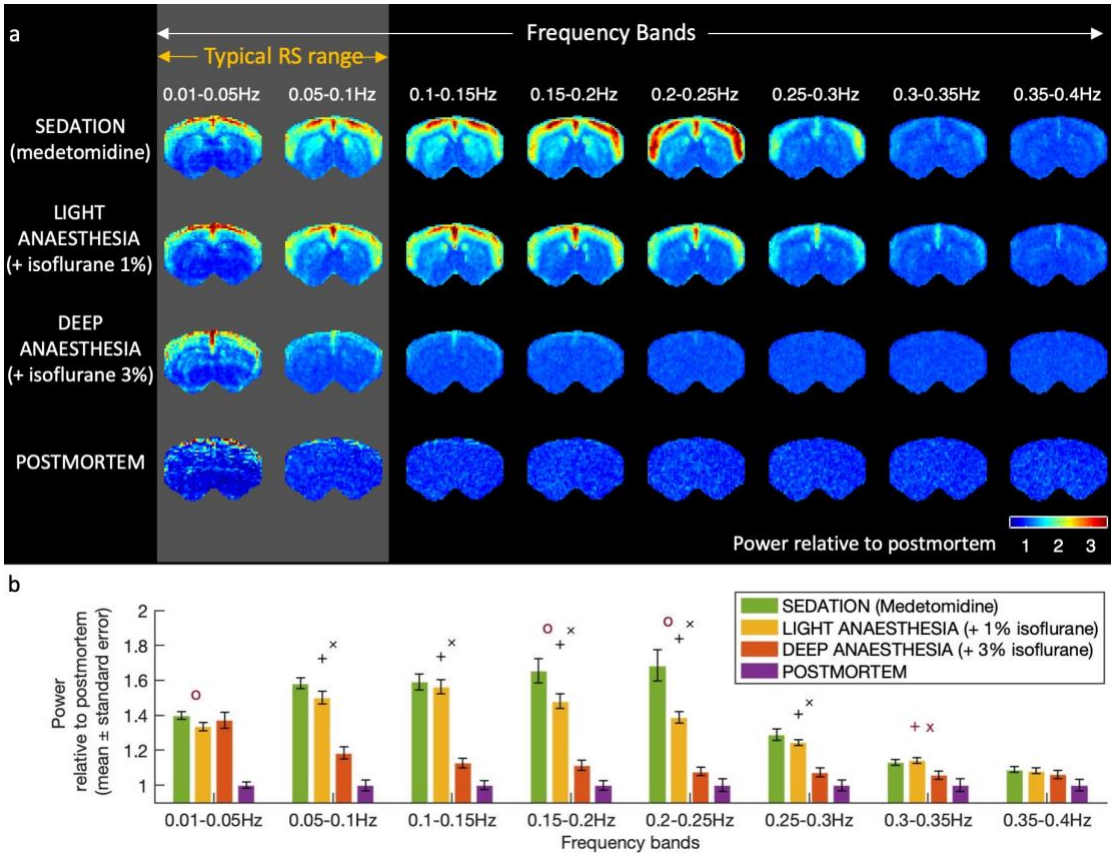


***Figure 2 – Oscillations in fMRI signals detected in brain voxels up to 0.3 Hz in sedated rats. A** – Spatial maps of spectral power averaged across all fMRI signals recorded from a frontal brain slice in each condition (power averaged across 12 scans/condition and normalized by the mean power in postmortem scans). **B** – Power across the 12 scans in each condition and in each frequency band relative to the mean power in postmortem scans. Error bars represent the standard error across scans in each condition. Symbols indicate statistical significance between: 'o' sedation vs light anaesthesia; '+' sedation vs deep anaesthesia; 'x' light vs deep anaesthesia. Black symbols indicate Bonferroni-corrected p-values for both the number of conditions and frequency bands compared (p<0.05/3/8), while red symbols survive correction only for the number of conditions compared (p<0.05/3). P-values reported in Fig. S3. RS, resting-state.*

bioRxiv preprint doi: https://doi.org/10.1101/2022.01.06.475200; this version posted January 6, 2022. The copyright holder for this preprint (which was not certified by peer review) is the author/funder, who has granted bioRxiv a license to display the preprint in perpetuity. It is made available under aCC-BY-NC-ND 4.0 International license.

While the space-frequency analysis provides information about which voxels have more power in each frequency band, it does not reveal how the phase of the oscillations organize in space. As can be seen in Video 1, the oscillations detected – particularly visible in in sedated animals - are not globally synchronized in phase, but instead exhibit characteristic phase relationships between voxels. Notably, synchronized activity is observed between distant voxels symmetrically aligned with respect to the vertical midline. In contrast, in deep anaesthesia, no particular spatial organization or fine structure could be detected, except for ultra-slow global fluctuations.

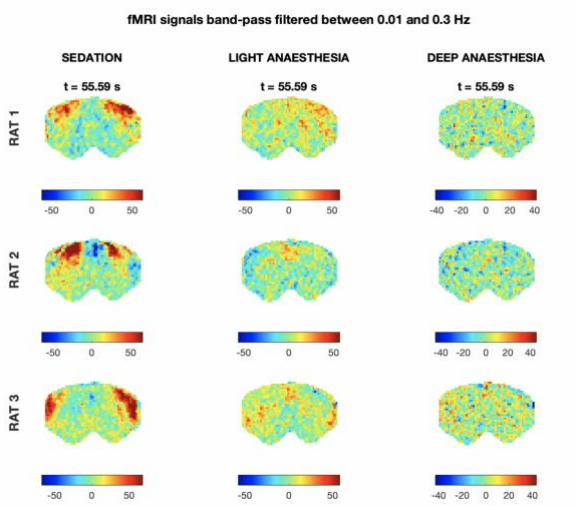


***Video 1 (still image)– fMRI signals band-pass filtered between 0.01 and 0.3 Hz in 3 different rats and in 3 different conditions (****Sedation: Medetomidine only; Light Anaesthesia: Medetomidine + 1% isoflurane; Deep anaesthesia: Medetomidine + 3% isoflurane). To account for expected differences in power across conditions, colorbar limits are set to $\pm 4$ standard deviations of the band-pass filtered signals in each scan.*

To characterize whether the oscillations have a characteristic spatial organization, we extract the principal components of the fMRI signals in each condition (see Methods for details). The spatial patterns associated with the 10 principal components detected above postmortem baseline reveal phase relationships between the fMRI signals in distinct brain subsystems (Figure 3d). These phase-relationships varying gradually and symmetrically across space exhibit characteristics of standing waves, where regions of strong amplitude represent the so-called 'anti-nodes'. Importantly, since standing waves are inherently associated with

bioRxiv preprint doi: https://doi.org/10.1101/2022.01.06.475200; this version posted January 6, 2022. The copyright holder for this preprint (which was not certified by peer review) is the author/funder, who has granted bioRxiv a license to display the preprint in perpetuity. It is made available under aCC-BY-NC-ND 4.0 International license.

resonance phenomena, their temporal signatures should exhibit oscillatory behavior, which is not a necessary property of principal components.

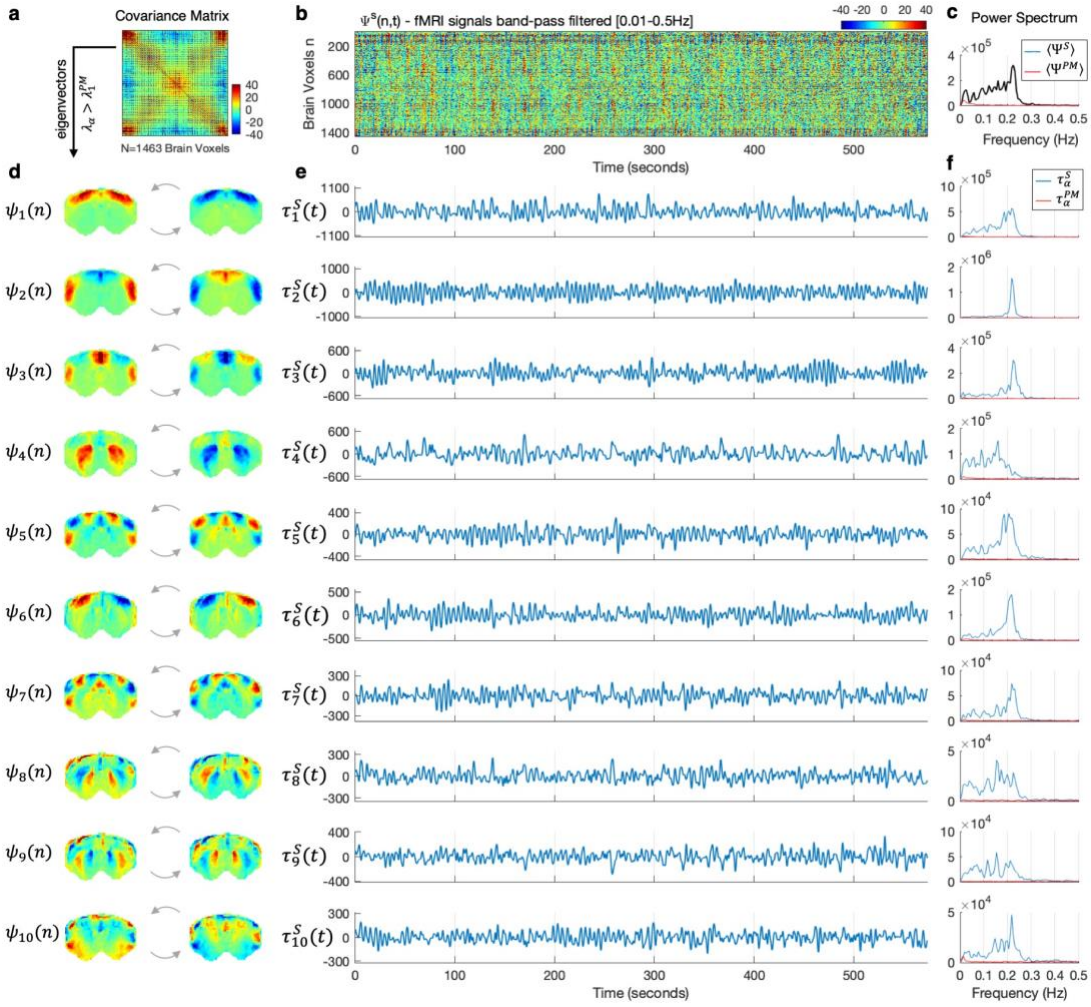


***Figure 3 – Principal components exhibit damped oscillatory behavior in medetomidine-sedated rats. a** – The NxN covariance matrix of fMRI signals between 0.01 and 0.3Hz, averaged across the 12 sedated rat scans **b** -The fMRI signals recorded in all brain voxels, n, over time, t, are represented by the wave function $\Psi^S(n,t)$, here shown for a representative scan **S** of a sedated rat in the frequency range [0.01-0.5Hz] **c** – Power spectrum of the mean fMRI signal across voxels for: (black) the scan shown in **b** and (red) a scan performed postmortem (**PM**). **d** – The 10 principal components $\psi_\alpha$ detected in medetomidine sedated rats with eigenvalue $\lambda_\alpha$ above baseline are scaled by 1 (left) and -1 (right) to illustrate the activity pattern when the temporal signature oscillates between positive and negative values. **e** – Temporal signature associated to each of the 10 principal components given by $\tau_\alpha^S(t) = \psi_\alpha(n)\Psi^S(n,t)$ for the same scan shown in **b**. Clear oscillations with fluctuating amplitude can be observed. **f** — Power spectra of the temporal signatures from **e** (blue) and in a postmortem scan (red)**.** See Video 2 for a dynamical representation of the principal components.*

We further investigate the oscillatory behavior of the putative standing waves detected. The temporal signature $\tau_\alpha^S(t)$ of each principal component $\alpha$ for scan *S* is obtained via: $\tau_\alpha^S(t) = \psi_\alpha(n)\,\Psi^S(n,t)$, where $\psi_\alpha(n)$ represents the spatial pattern of each principal component $\alpha$ and $\Psi^S(n,t)$ represents the activity recorded with fMRI across all voxels *n* and

bioRxiv preprint doi: https://doi.org/10.1101/2022.01.06.475200; this version posted January 6, 2022. The copyright holder for this preprint (which was not certified by peer review) is the author/funder, who has granted bioRxiv a license to display the preprint in perpetuity. It is made available under aCC-BY-NC-ND 4.0 International license.

timepoints $t$ for scan $S$ (Figure 3b, c.f. Figs. S6-9 for carpet plots of $\Psi^S$ in different conditions and different frequency ranges).

Given that the principal components are orthogonal by definition - and henceforth obeying the general wave superposition principle - the reconstruction $\Psi^R(n,t) = \sum_{\alpha=1}^{10} \psi_\alpha(n)\tau_\alpha^S(t)$ describes the linear superposition of a reduced basis of wave patterns locked in space $\psi_\alpha(n)$ – and evolving in time $\tau_\alpha^S(t)$. In Video 2, we show how the macroscopic dynamics of the activity recorded from a rat brain are captured from the 10 temporal signatures $\tau_\alpha^S(t)$ associated with the reduced common basis of 10 principal components $\psi_\alpha(n)$ detected across sedated rats.

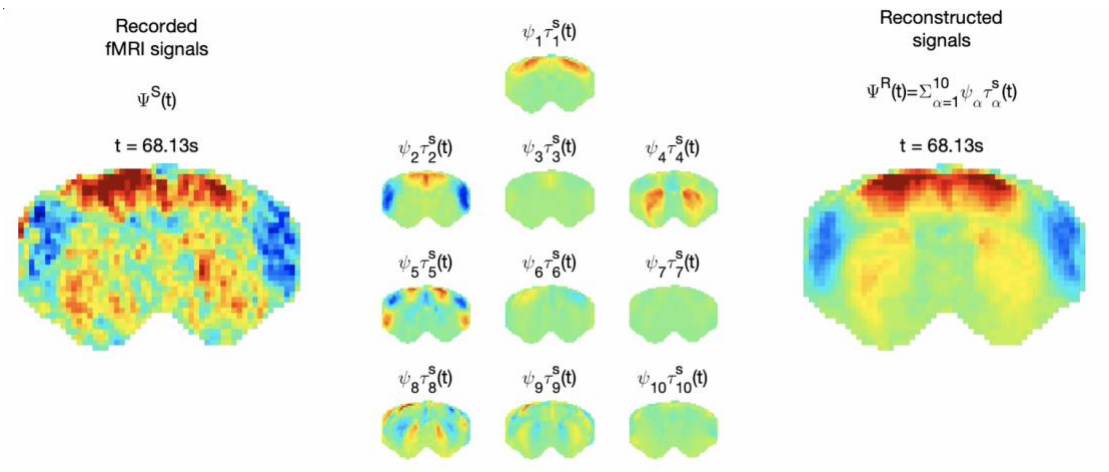


***Video 2 (still image)– Reconstruction of a representative fMRI recording as the superposition of 10 condition-specific principal components with scan-specific temporal signatures. (left)*** *fMRI signals band-pass filtered between 0.01 and 0.3 Hz recorded from a representative rat under medetomidine only.* ***(middle)*** *Each of the 10 principal components obtained from the covariance matrix averaged across all 12 sedated rats scans is scaled by the associated scan-specific temporal signature.* ***(Right)*** *To account for differences in power across components, colorbar limits are set to $\pm 4$ standard deviations of the temporal signatures.*

As observed in **Figure 3** and **Video 2**, the principal components are found to oscillate around the mean, generating patterns akin to those of vibrating standing waves. Notably, the oscillations display slowly fluctuating amplitudes. This transiently sustained periodicity is reflected in the resonant peaks emerging clearly in the associated power spectra (**Figure 3f**).

With the addition of isoflurane at 1% concentration (**Figure 4** top), the repertoire of principal components is modified, not only in number (with only 6 components detected

bioRxiv preprint doi: https://doi.org/10.1101/2022.01.06.475200; this version posted January 6, 2022. The copyright holder for this preprint (which was not certified by peer review) is the author/funder, who has granted bioRxiv a license to display the preprint in perpetuity. It is made available under aCC-BY-NC-ND 4.0 International license.

above the postmortem baseline) but also in terms of spatial configuration, with different brain subsystems exhibiting in-phase or anti-phase synchronization. Additionally, the distribution of power becomes broader with multiple peaks at lower frequencies (**Figure 4f**). This is particularly visible in the temporal signature of mode $\psi_2$ in **Figure 4e**, where transient oscillations can be seen to emerge with different periodicity over time, unlike the sustained periodicity observed with medetomidine sedation in **Figure 3e.**

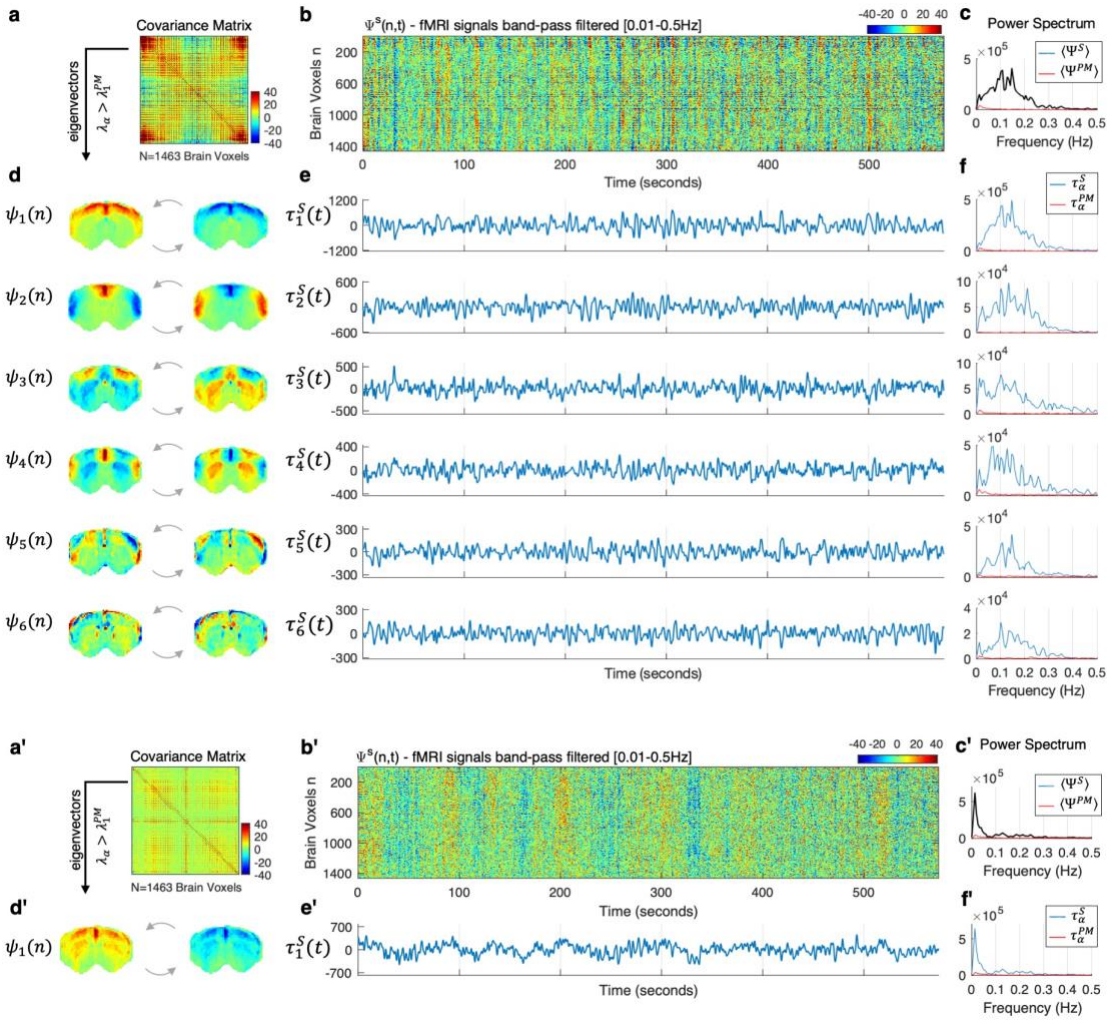


***Figure 4 – The addition of isoflurane at 1% and 3 % concentrations alters the spatial, temporal, and spectral signatures of principal components. (a,a')*** *The NxN covariance matrix of fMRI signals band-pass filtered between 0.01 and 0.3Hz, averaged across 12 scans after the addition of isoflurane at 1%* ***(top)*** *and 3%* ***(bottom)*** *concentrations. (**b,b'**) The fMRI signals recorded in all brain voxels, n, over time, t, represented by the wave function $\Psi^S(n,t)$, here shown for two scans S of the same rat from Figure 3 in the frequency range [0.01-0.5Hz]. (**c,c'**) – Power spectrum of the mean fMRI signal across voxels. (**d,d'**) The principal components detected with eigenvalue above baseline are scaled by 1 (left) and -1 (right) to illustrate the activity pattern when the temporal signature oscillates between positive and negative values. (**e,e'**) Temporal signature associated to each of the supra-threshold principal components given by $\tau_\alpha^S(t) = \psi_\alpha(n)\Psi^S(n,t)$ for the same scan shown in **b**. (**f,f'**) Power spectra of the temporal signatures from **e.***

bioRxiv preprint doi: https://doi.org/10.1101/2022.01.06.475200; this version posted January 6, 2022. The copyright holder for this preprint (which was not certified by peer review) is the author/funder, who has granted bioRxiv a license to display the preprint in perpetuity. It is made available under aCC-BY-NC-ND 4.0 International license.

When the concentration of isoflurane is further increased to 3% (**Figure 4** bottom), the variance above postmortem baseline is explained by a single principal component, oscillating with strong power at a very low frequency. These slow global oscillations are particularly visible in **Figure 4**b'.

Our observations provide insight into the mechanisms driving spontaneous long-range correlations. Despite the difference in number, spatial configuration and peak frequency, the principal components detected with fMRI between 0.01 and 0.3 Hz are qualitatively similar across conditions, indicating they likely represent a common generative principle. Our hypothesis is that they represent distinct resonant modes emerging from the same system (the brain) under different control parameters (medetomidine and isoflurane). Generally, the resonant modes of a system depend not only on the structural shape of the system (which in this case can be assumed to remain invariant across conditions), but also on the resistivity of the propagating medium, which directly affects not only the spatial patterns, but also the resonant frequency and the stability of the oscillations.

In **Figure 5** we show the peak frequency and stability of the oscillations associated to each principal component in each scan. The stability of the oscillations is assessed from the resonance Q-factor, which is a metric used to evaluate a system's resonant quality, being proportional to the number of cycles before the amplitude decays to ~37% ($e^{-1}$) of its initial value, consisting in the ratio between the peak frequency and the power spectrum's full-width-at-half-maximum (FWHM). Both the peak frequencies and the Q-factors were found to be significantly higher in sedation and light anaesthesia with respect to deep anaesthesia (Bonferroni-corrected p-values reported in Table S2).

bioRxiv preprint doi: https://doi.org/10.1101/2022.01.06.475200; this version posted January 6, 2022. The copyright holder for this preprint (which was not certified by peer review) is the author/funder, who has granted bioRxiv a license to display the preprint in perpetuity. It is made available under aCC-BY-NC-ND 4.0 International license.

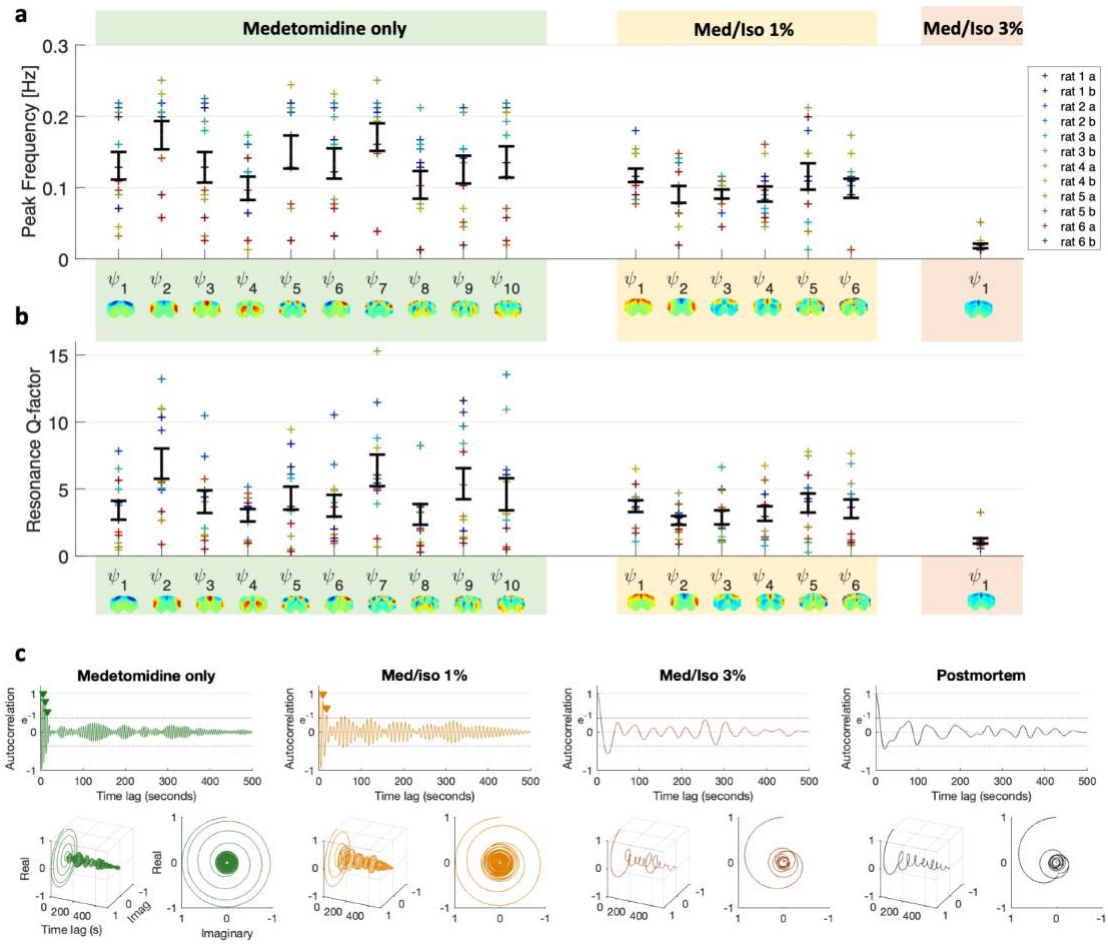


***Figure 5 – Principal components oscillate at higher frequencies and with less damping under medetomidine. (a,b)*** *The temporal signatures associated to the principal components detected in each condition are characterized in terms of peak frequency and Q-factor for each of the 12 scans in each condition (2 scans per rat per condition). Errorbars represent the mean $\pm$ standard error across scans. Statistics reported in Table S2.* ***(c)*** *To illustrate the stability of the oscillations, the temporal signatures $\tau_1^S$ associated to the first principal component in each condition are filtered around the peak frequency and the autocorrelation functions computed. Examples are shown for 3 scans form the same rat and the same obtained from a postmortem scan. As can be seen, the autocorrelation function under medetomidine exhibits 3 oscillations before the amplitude decays to 1/e (~37%), 2 cycles after adding isoflurane at 1% and no complete cycle under deep anaesthesia, similar to what is observed in the postmortem scan.*

Analyzing the autocorrelation function of the temporal signature $\tau_\alpha^S(t)$ associated to the first principal component detected across conditions in the same rat (**Figure 5**c), we observe that the number of sustained cycles before the autocorrelation decays to $e^{-1}$ decreases with increasing levels of isoflurane, as predicted by the Q-factor.

In physics, the presence of a damped oscillation in the autocorrelation function indicates that, whenever the system is deviated from a fixed-point equilibrium, it returns to equilibrium with an oscillation, ensuring the conservation of angular momentum. To illustrate

bioRxiv preprint doi: https://doi.org/10.1101/2022.01.06.475200; this version posted January 6, 2022. The copyright holder for this preprint (which was not certified by peer review) is the author/funder, who has granted bioRxiv a license to display the preprint in perpetuity. It is made available under aCC-BY-NC-ND 4.0 International license.

the conservation of angular momentum, we transform the autocorrelation signals into their analytic representation in complex coordinates using the Hilbert transform (**Figure 5**c bottom). The phase portraits of the autocorrelation function in the sedation and light anaesthesia scans reveal a clear 'spiral sink attractor', indicative that the standing waves exhibit an underdamped response (see illustration in **Figure 6A green**). Notably, noisy perturbations to an underdamped system (**Figure 6**B green) induce transient oscillations at the natural frequency (here simulated using the Stuart-Landau equation with $\omega_0 = 0.22$ Hz) with the real part closely approximating the wave temporal signatures reported in **Figure 3** for rats under medetomidine. Further increasing the damping suppresses the frequency-specificity and the oscillations become hardly distinguishable from aperiodic fluctuations (**Figure 6**C).

To expand our results obtained in a single slice to the whole-brain level, the principal components were obtained from six 15-minute-long fMRI scans covering 12 brain slices of 3 medetomidine sedated rats. Despite the necessarily lower temporal resolution of multi-slice acquisitions (here TR= 350 ms), oscillations could still be clearly detected (see Video 3) revealing covariance patterns that overlap with the ones detected in the frontal slice of ultrafast fMRI recordings (c.f. Figs. S10-S11), supporting the hypothesis that the conclusions drawn from the single slice ultrafast acquisitions can be expanded to the whole-brain level. However, the limited temporal resolution affects the power spectrum at higher frequencies (cf. Figs. S12-13), such that even in the fMRI scan that exhibited most power >0.15Hz, the frequency-specificity is much lower than the one observed in single-slice acquisitions (see Fig. S14). The principal components detected from the average covariance matrix across the 6 whole brain scans are rendered in 3-D (view from top) in Figure 6E.

bioRxiv preprint doi: https://doi.org/10.1101/2022.01.06.475200; this version posted January 6, 2022. The copyright holder for this preprint (which was not certified by peer review) is the author/funder, who has granted bioRxiv a license to display the preprint in perpetuity. It is made available under aCC-BY-NC-ND 4.0 International license.

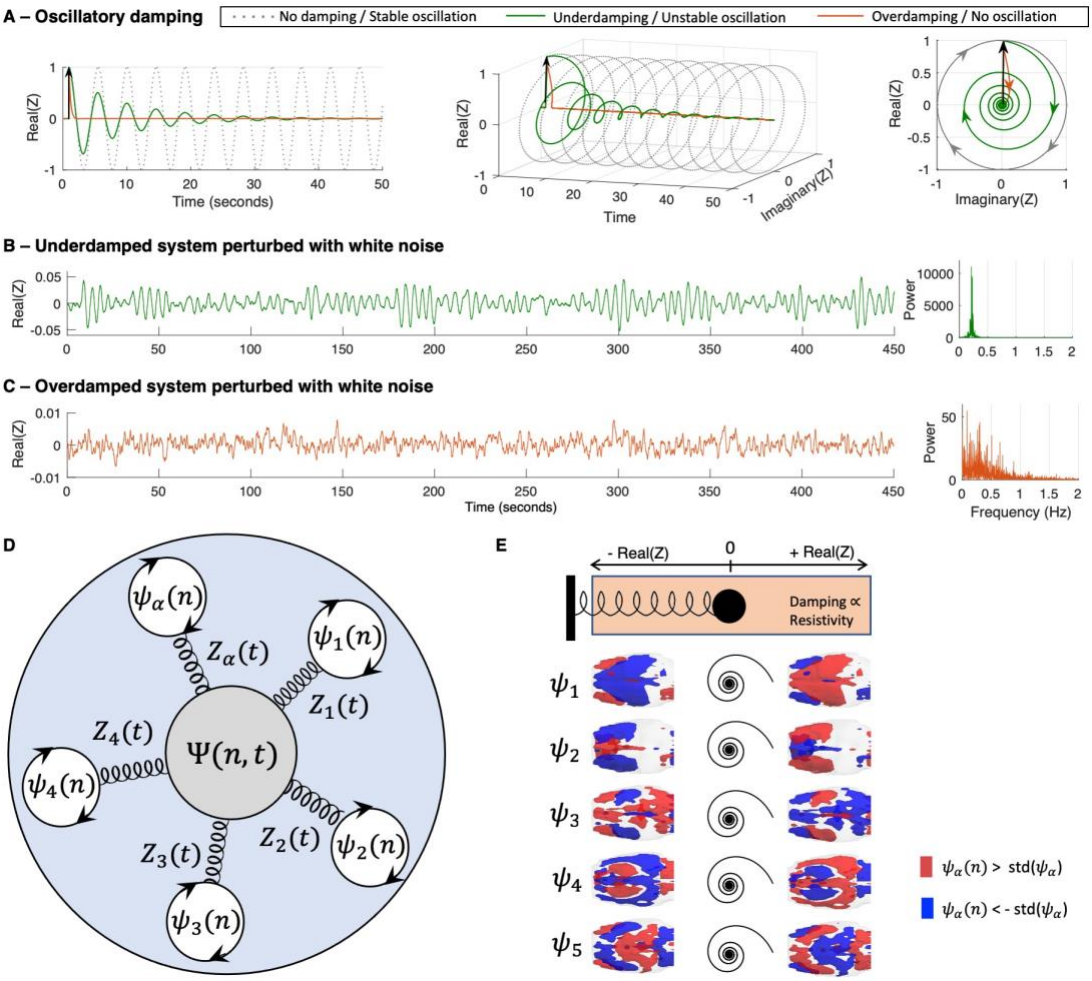


***Figure 6 – Mechanistic model for the spontaneous resonance of standing waves driving the activation of functional brain networks. A*** *– Illustration of 3 regimes of harmonic motion through numerical integration of a Hopf oscillator (**Error! Reference source not found.**) in response to a unit pulse added at t = 1 s with $\omega_0$ = 0.22 Hz and α = 1 (no damping, dashed grey), α = -0.1 (underdamping, green) and α =-2 (overdamping, red). Since Z has an imaginary component – to allow for the conservation of angular momentum - 3 perspectives of the same plot are reported in left, middle and right panels. **B,C** – Simulation of a Hopf oscillator with natural frequency $\omega_0$ = 0.22 Hz in the underdamped (B) and overdamped (C) regimes in the presence of Gaussian white noise and corresponding power spectra. **D** — Diagram illustrating a mechanistic scenario for brain activity, where each functional network is represented by a spatial pattern $\psi_\alpha$ responding to perturbation with a damped oscillation. **E** - Similar to the damped oscillatory response of a spring, the temporal signature of brain modes can be approximated by the real part of a Hopf oscillator. Despite the lower temporal resolution inherent to multi-slice acquisitions hindering the detection of resonant behavior, we hypothesize that the underdamped response of functional networks extends to the whole-brain level, here represented by the first 5 eigenvectors of the average covariance matrices across 6 whole-brain scans.*

bioRxiv preprint doi: https://doi.org/10.1101/2022.01.06.475200; this version posted January 6, 2022. The copyright holder for this preprint (which was not certified by peer review) is the author/funder, who has granted bioRxiv a license to display the preprint in perpetuity. It is made available under aCC-BY-NC-ND 4.0 International license.

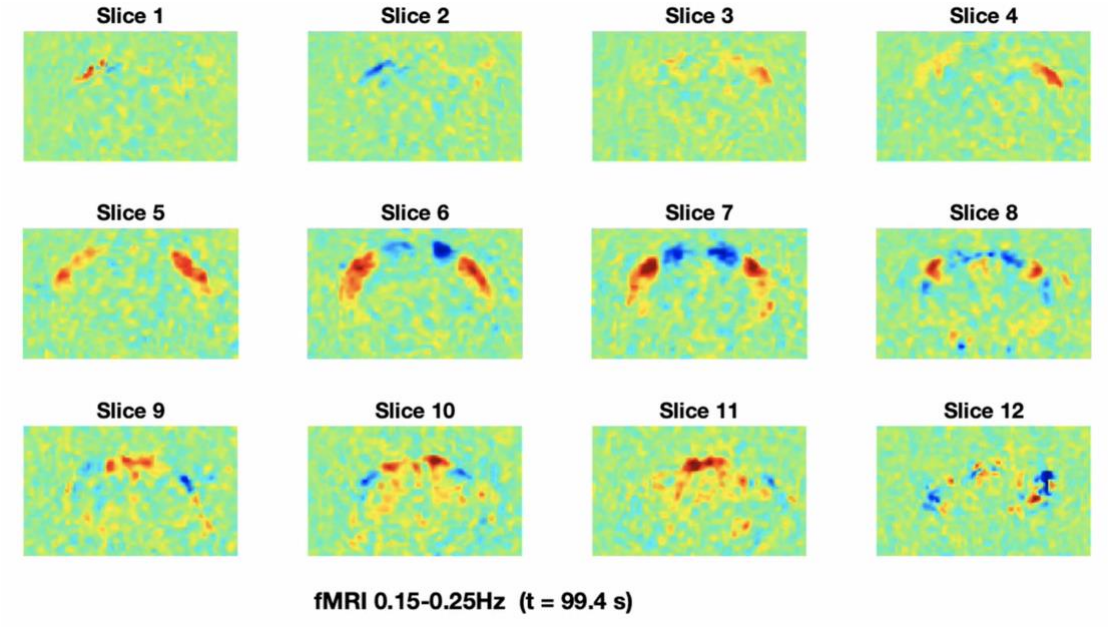


***Video 3 (still image) – Multi-slice acquisitions reveal that the patterns detected in the frontal slice extend to the whole brain level.*** *fMRI signals recorded from a rat sedated with medetomidine with TR=0.350 seconds from 12 slices covering the whole brain (anterior to posterior) filtered between 0.15-0.25 Hz (no other signal processing performed).*

In summary, the clear frequency-specific oscillations exhibited by the distinct principal components of fMRI signals reinforces the hypothesis that they represent standing waves emerging from resonance phenomena within the brain's anatomical structure. Moreover, these findings reveal that fluctuations in sliding-window correlation are associated with the transient resonance of standing waves, which drive transiently synchronized activity between the brain subsystems located at the standing wave anti-nodes.

bioRxiv preprint doi: https://doi.org/10.1101/2022.01.06.475200; this version posted January 6, 2022. The copyright holder for this preprint (which was not certified by peer review) is the author/funder, who has granted bioRxiv a license to display the preprint in perpetuity. It is made available under aCC-BY-NC-ND 4.0 International license.

# Discussion

Rhythms at frequencies ranging from 0.5 up to >100 Hz have been shown to emerge from intrinsic neural processes (*30-32*). However, the role and generative mechanisms of rhythms below 0.5 Hz detected both with fMRI, EEG and electrophysiology remain under vigorous debate (*6, 8, 18, 22, 33*). Despite the traditionally low temporal resolution of fMRI studies (typically above 1 sec), whole brain coverage at high spatial resolution has allowed for network-based analysis of ultra-slow fluctuations, revealing consistent large-scale organization into functional networks (*9-11, 34*), as expressed via correlations measured between the signals in distant areas. More recently, dynamic analysis of functional connectivity has revealed the non-stationary nature of network interactions (*14, 35, 36*). Still, under the *Connectomics* framework, even dynamic studies measure spatial connectivity patterns over time, rather than investigating deeper origins of the ultraslow signals. Conflicting hypotheses have been put forth on the nature of the functional connectivity, ranging from aperiodic co-activations (*37-39*), metastable synchronization (*40, 41*), superposition of harmonic modes (*42, 43*) or transitions between phase-locking patterns (*44, 45*), but with little evidence to support a conclusion on either end of the spectrum.

Using fMRI experiments with hitherto unprecedented temporal resolution we were able to provide new insights into this problem and demonstrate that functional network patterns are underpinned by distinct resonant modes (i.e., three-dimensional standing waves) emerging within spatially defined cortical and subcortical boundaries. Resonance is a universal principle governing self-organized oscillations in bounded dynamical systems. Each resonant mode is associated with the stability of a particular spatial organization of the system into a dynamical mode with poles (or anti-nodes) and zeros, driving synchronized 'activity' across regions of the system with shared polarity. This resonance framework offers simultaneously an explanation for the spontaneous emergence of ultra-slow oscillations in brain activity and

bioRxiv preprint doi: https://doi.org/10.1101/2022.01.06.475200; this version posted January 6, 2022. The copyright holder for this preprint (which was not certified by peer review) is the author/funder, who has granted bioRxiv a license to display the preprint in perpetuity. It is made available under aCC-BY-NC-ND 4.0 International license.

for the profile of phase relationships across space. A closer observation of the spatial modes in Figure 3 reveals that some may represent fundamental modes of specific brain structures (i.e., $\psi_1$ for the cortex, $\psi_4$for the striatum), whereas others represent their harmonics (i.e., $\psi_{6,2,3,5,7}$ for the cortex, $\psi_8$ for the striatum). Although a rigorous validation would require computing the exact Laplace eigenfunctions considering the complex brain structure, including anatomical resistivity and fluid viscosity, these observations corroborate previous studies proposing (through approximate calculations) that resting-state networks are the expression of different harmonic modes of the brain (*42, 43, 46, 47*).

The general principle of wave superposition implies that the brain can engage simultaneously in multiple functional networks, instead of switching from one functional network to another, as often considered in the analysis of dynamic functional connectivity (*45, 48-50*). In other words, our results substantiate that activity recorded with fMRI aligns with field theories proposed for electromagnetic brain activity (*51-53*), where at any given moment t, the wave function $\Psi(t)$ represents the collective entity resulting from the linear sum of multiple non-interacting wave functions.

The temporal signatures of the principal components reveal properties of underdamped systems, where noise induces frequency-specific oscillations with fluctuating amplitude (*54*). In dynamical systems theory, such systems are said to be in the vicinity of a Poincaré-Andronov-Hopf (or simply Hopf) bifurcation, which represents the transition between a fixed point to a limit-cycle equilibrium, and can be described mathematically by the Stuart-Landau equation (*54, 55*). This equation has been used in previous models of resting-state activity to represent local field oscillations interacting through the connectome structure (*44, 56, 57*). Here instead, we propose that oscillations are not locally generated but associated to the vibration of spatially-defined wave patterns. This reduction is intended at linking the observed phenomena with the theory of dynamical systems, which can help

bioRxiv preprint doi: https://doi.org/10.1101/2022.01.06.475200; this version posted January 6, 2022. The copyright holder for this preprint (which was not certified by peer review) is the author/funder, who has granted bioRxiv a license to display the preprint in perpetuity. It is made available under aCC-BY-NC-ND 4.0 International license.

deciphering the most fundamental principles driving the complex dynamical patterns observed in brain activity.

The resonant quality of covariance modes was found to be modulated by anesthetics. Notably, isoflurane at 1% concentration was found to particularly suppress oscillations between 0.15 and 0.25 Hz, but to keep high power in the typical range considered in resting-state studies (i.e. < 0.1 Hz). Further increasing isoflurane concentration to 3%, only globally synchronized and very slow oscillations are detected. However, it remains unclear whether these non-linear effects are related with the differential effects of medetomidine and isoflurane on blood vessels or can be explained by more direct changes in the resistivity of the medium through which the waves propagate.

A question that typically arises in this context is how closely the fMRI signals track the underlying neural activity, mainly due to the involvement of neurovascular coupling mechanisms. Although this study did not attempt to de-confound neural activity from vascular coupling, it is interesting to note that the mode temporal signatures did not follow the canonical hemodynamic response function. Instead, a ubiquitous transiently sustained periodicity occurs within a range of frequencies extending significantly above the range typically associated to the Blood Oxygenation Level Dependent signal (i.e., <0.1 Hz). Furthermore, recent studies combining simultaneous local electrophysiological recordings and fMRI in rats reported significant (phase-lagged) coherence between the two signals precisely in the range of frequencies detected herein (*19, 20*). Therefore, one cannot exclude the possibility that the oscillations here observed with fMRI have a physiological origin distinct from purely blood flow/volume effects, reinforcing the need to further explore the origin of resting-state fMRI signals (*5*).

Finally, the extrapolation of these findings to other animal species including humans can only be discussed in the light of existing literature. The similarity of the spatial patterns

bioRxiv preprint doi: https://doi.org/10.1101/2022.01.06.475200; this version posted January 6, 2022. The copyright holder for this preprint (which was not certified by peer review) is the author/funder, who has granted bioRxiv a license to display the preprint in perpetuity. It is made available under aCC-BY-NC-ND 4.0 International license.

detected herein with known intrinsic networks detected with fMRI not only in rats (*26*) but also in humans (*11*), suggests some generalizability of the phenomenon across species. Indeed, resting-state networks in humans have been shown to be associated to macroscopic 'phase-locking' patterns, emerging transiently and recurrently across subjects (*58-60*). Moreover, although the temporal signatures of resting-state networks in humans have not been reported to exhibit fine-tuned oscillations, it is possible that the fluctuations detected in the relatively narrow frequency range between 0.01 and 0.1 Hz are the signature of overdamped oscillatory responses, in which case they can hardly be distinguished from aperiodic fluctuations. Importantly, hypothesis-driven analysis to human resting-state fMRI data is crucial to verify the scale at which of the results reported herein can be extended to humans.

To conclude, this work presents ubiquitous evidence of oscillations detected in fMRI signals that organize across the brain in standing wave patterns, providing fresh insight into the self-organizing principles giving rise to resting-state networks. Moreover, it shows that the field theory previously used for describing electromagnetic brain activity can be extended to explain the signals detected with fMRI. Future work disentangling the origin of fMRI signals at the whole-brain level, as well as studying the impact of specific therapeutic effects, such as direct electromagnetic stimulation or pharmacological manipulations, should deepen our understanding of resonant fields in the brain.

## Methods

### *Experimental Design*

All animal experiments followed the European Directive 2010/63 and were preapproved by the Institution's Review Board and the national competent authority.

bioRxiv preprint doi: https://doi.org/10.1101/2022.01.06.475200; this version posted January 6, 2022. The copyright holder for this preprint (which was not certified by peer review) is the author/funder, who has granted bioRxiv a license to display the preprint in perpetuity. It is made available under aCC-BY-NC-ND 4.0 International license.

Ultrafast resting-state fMRI recordings were obtained from a single brain slice of 6 rats scanned under 3 different conditions, namely medetomidine (*27*) combined with 3 concentrations of isoflurane: 0% (sedation), 1% (light anaesthesia) and 3% (deep anaesthesia). Two additional postmortem scans were recorded from a seventh rat to serve as baseline. Moreover, resting-state fMRI recordings covering 12 slices of the rat brain were acquired from 3 rats under medetomidine. Below, we elaborate on each phase.

### *Animal preparation*

Long-Evans female rats (*N*=6) weighing 206 ± 16 g and aged 8.3 ± 1.3 weeks were used in this study. Animals were reared in a temperature-controlled room and held under a 12h/12h light/dark cycle with *ad libitum* access to food and water.

Anaesthesia was induced with 5% isoflurane (Vetflurane™, Virbac, France) mixed with oxygen-enriched (27-30%) air in a custom-built plastic box. Rats were then weighed, moved to the animal bed (Bruker, Germany) and isoflurane was reduced to 2.5%. Eye ointment (Bepanthen Eye Drops, Bepanthen, Germany) was applied to prevent eye dryness. A 0.05 mg/kg bolus of medetomidine solution (Dormilan, Vetpharma Animal Health, Spain: 1 mg/ml, diluted 1:10 in saline) was injected subcutaneously 5-8 min after induction, immediately followed by a constant infusion of 0.1 mg/kg/h s.c. of the same solution (*25*), delivered via a syringe pump (GenieTouch™, Kent Scientific, USA) until the end of the experiment, and by a 10 min-long period where isoflurane was gradually decreased to 0%. fMRI acquisitions began once the animals stabilized in this condition (the time after isoflurane is reported in Table S1 for each scan). For each rat, 2 fMRI scans were first acquired under medetomidine only (sedation condition). Subsequently, fMRI scans were acquired after increasing isoflurane concentration to 1% (light anaesthesia condition) and finally to 3% (deep anaesthesia condition), waiting 10 min after each isoflurane increase for anaesthesia stabilization.

bioRxiv preprint doi: https://doi.org/10.1101/2022.01.06.475200; this version posted January 6, 2022. The copyright holder for this preprint (which was not certified by peer review) is the author/funder, who has granted bioRxiv a license to display the preprint in perpetuity. It is made available under aCC-BY-NC-ND 4.0 International license.

The breathing frequency and rectal temperature were monitored throughout the MRI sessions using a pillow sensor and an optic fiber probe (SA Instruments Inc., Stony Brook, USA), respectively. In the end of the experiments, medetomidine sedation was reverted by injecting 0.25 mg/kg s.c. of atipamezole (Antisedan, Vetpharma Animal Health, Spain: 5 mg/ml, diluted 1:10 in saline).

A seventh rat, reared in the same conditions, was injected with 1 mL (60 mg) pentobarbital i.p. and scanned postmortem with the same MRI protocol to serve as a control.

### *MRI protocol*

Animals were imaged using a 9.4 T BioSpec® MRI scanner (Bruker, Germany) equipped with an AVANCE™ III HD console, producing isotropic pulsed field gradients of up to 660 mT/m with a 120 µs rise time. RF transmission was achieved using an 86 mm-ID quadrature resonator, while a 4-element array cryoprobe (Bruker, Fallanden, Switzerland) was used for signal reception. Following localizer experiments and routine adjustments for centre frequency, RF calibration, acquisition of $B_0$ maps and automatic shimming, anatomical images were acquired using a $T_2$-weighted RARE sequence in the coronal plane: TR/TE = 2000/36 ms, FOV = 18 x 16.1 mm$^2$, in-plane resolution = 150 x 150 µm$^2$, RARE factor = 8, slice thickness = 0.6 mm, 22 slices, $t_{acq}$ = 3 min 28 s, and sagittal plane: TR/TE = 2000/36 ms, FOV = 24 x 16.1 mm$^2$, in-plane resolution = 150 x 150 µm$^2$, RARE factor = 8, slice thickness = 0.5 mm, 20 slices, $t_{acq}$ = 3 min 28 s. These images were used to place the slices of interest.

### *Single-slice ultrafast fMRI acquisitions*

To minimize the repetition time, we focused our analysis in a single 1.2 mm-thick slice of the rat brain, choosing a frontal slice that covered a large cortical area and with a FOV of 21 x 21 mm$^2$, as shown in Fig. S1 A-B. The slice was placed between -0.2 and 1.0 mm from Bregma according to the Paxinos & Watson rat brain atlas (*61*) (Fig. S1 C). Six resting-state scans (2 per condition) were acquired from each of *N*=6 living rats (totaling 36 scans) using a gradient-echo

bioRxiv preprint doi: https://doi.org/10.1101/2022.01.06.475200; this version posted January 6, 2022. The copyright holder for this preprint (which was not certified by peer review) is the author/funder, who has granted bioRxiv a license to display the preprint in perpetuity. It is made available under aCC-BY-NC-ND 4.0 International license.

echo planar imaging (GE-EPI) sequence (TR/TE = 38/11 ms, flip angle = 15°, matrix size = 84 x 84, in-plane resolution = 250 x 250 µm$^2$, number of time frames = 16000, $t_{acq}$ = 10 min 8 s). Two postmortem scans were acquired with the same parameters. Additionally, a Multi-Gradient Echo sequence (MGE, TE = 2.5:5:97.5 ms, TR = 300 ms, flip angle = 40°, matrix size = 210 x 210, in-plane resolution = 100 x 100 µm$^2$, $t_{acq}$ = 4 min 12 s) and a Time-Of-Flight (TOF) FLASH sequence (TR/TE = 8.2/3.3 ms, flip angle = 80°, matrix size = 210 x 210, in-plane resolution = 100 x 100 µm$^2$, $t_{acq}$ = 17 s 219 ms) sequence were acquired from all rats to obtain additional anatomical and vascular information about the slice, respectively. Details of time after isoflurane induction, breathing frequency and rectal temperature are reported for each scan in Table S1.

### *Brain mask*

Individual brain masks were defined manually and aligned across rats to a common central coordinate. All individual rat masks were superposed to define a common brain mask containing *N*=1463 voxels. Importantly, no interpolation was applied to the signals, such that the signal in each brain voxel corresponds to the raw fMRI signals recorded.

### *Whole-brain fMRI acquisitions*

Resting-state data was also acquired twice under medetomidine sedation from *N*=3 rats using a multi-slice GE-EPI sequence covering the entire rat brain, from the frontal part of the cerebellum to the posterior part of the olfactory bulb, and with the following parameters: TR/TE = 350/11 ms, flip angle = 40°, FOV = 24 x 24 mm$^2$, matrix size = 70 x 70, in-plane resolution = 342.9 x 342.9 µm$^2$, slice thickness = 1.2 mm, slice gap = 0.15 mm, 12 slices, number of time frames = 2572, $t_{acq}$ = 15 min 0 s 200 ms.

bioRxiv preprint doi: https://doi.org/10.1101/2022.01.06.475200; this version posted January 6, 2022. The copyright holder for this preprint (which was not certified by peer review) is the author/funder, who has granted bioRxiv a license to display the preprint in perpetuity. It is made available under aCC-BY-NC-ND 4.0 International license.

### *Space-frequency analysis of fMRI data*

Power spectra were computed for the fMRI signals on each of the 84 x 84 = 7056 voxels using the fast Fourier transform, after removing the first 500 frames (19 seconds) and detrending. Voxel power spectra were obtained up to the Nyquist frequency of $(2TR)^{-1}$ = 13.1579 Hz. Images of the power across a selected range of frequencies were obtained by averaging the band-limited power in each voxel across scans in the same condition. All spectral analyses were performed at the single scan level and metrics statistically compared between conditions. Analysis up to the Nyquist frequency are reported in Supplementary section I and

### *Principal Component analysis*

For each scan, the fMRI signals in $N = 1463$ brain voxels were band-pass filtered between 0.01 and 0.3Hz and the $NxN$ covariance matrix was computed. The largest magnitude eigenvalue, $\lambda_1^{PM}$ was calculated for the two postmortem scans, and the largest one selected as the baseline threshold. The covariance matrices were averaged across the 12 scans in each condition, and, for each condition the $\alpha$ eigenvectors with eigenvalue $\lambda_\alpha^{condition} > \lambda_1^{PM}$ were extracted, representing the principal components detected in each condition with magnitude above the postmortem baseline.

### *Statistical analysis*

We compared the power between conditions at different frequency bands using a non-parametric permutation-based t-test (10 000 permutations to ensure robustness of results) to detect the frequency range most sensitive to the 3 different conditions. P-values were conservatively corrected by the number of comparisons performed (Bonferroni correction), considering both the number of between-group comparisons (considering only independent hypotheses) as well as the number of frequency bands considered (considering dependent hypotheses as well, which is more conservative).

bioRxiv preprint doi: https://doi.org/10.1101/2022.01.06.475200; this version posted January 6, 2022. The copyright holder for this preprint (which was not certified by peer review) is the author/funder, who has granted bioRxiv a license to display the preprint in perpetuity. It is made available under aCC-BY-NC-ND 4.0 International license.

The resonance Q factors and peak frequencies were statistically compared using the same permutation test.

Standard error is calculated as the standard deviation divided by the square root of the number of values compared.

### *Resonance analysis*

Resonance was evaluated by computing the Q-factor, a measure typically used in acoustics and engineering to quantify resonance phenomena. Importantly, it is not implied by definition that a covariance mode will oscillate, since signals can co-vary aperiodically, without necessarily oscillating. In Figure 2 in the main manuscript, the Q-factors (mean and standard deviation) of 10 covariance mode are reported and statistically compared between groups (p-values reported in Table S2). In Fig. S11 we report the mean Q-factors (averaged across rats in the same condition) associated to the 76 covariance modes detected across the 8 frequency bands analyzed in Figure 1.

### *Damped Oscillator Model*

To illustrate the response of an oscillatory system with different damping coefficients, we used the Stuart-Landau equation:

$$\frac{dZ}{dt} = Z(i\omega - |Z^2| + a)$$

where $Z$ is complex (with real and imaginary components), $\omega$ is the natural frequency, and '$a$' defines the position of the system with respect to the bifurcation at $a = 0$, such that for $a > 0$ the system displays self-sustained oscillations with constant amplitude scaled by $a$, whereas for $a < 0$ the oscillations are damped and the system decays back to the fixed point at $Z = 0$ at a rate scaled by the magnitude of $a$ (i.e., the more negative the $a$, the stronger the damping).

bioRxiv preprint doi: https://doi.org/10.1101/2022.01.06.475200; this version posted January 6, 2022. The copyright holder for this preprint (which was not certified by peer review) is the author/funder, who has granted bioRxiv a license to display the preprint in perpetuity. It is made available under aCC-BY-NC-ND 4.0 International license.

A single unit pulse (i.e., a Dirac delta function) was applied at t=0 to illustrate the intrinsic response of the system. Further, to illustrate the response to continuous perturbation with a stochastic input, we add complex Gaussian white noise as:

$$\frac{dZ}{dt} = Z(i\omega - |Z^2| + a) + \beta\eta_1 + i\beta\eta_2,$$

where $\eta_1$ and $\eta_2$ are independently drawn from a Gaussian distribution with standard deviation $\beta = 1$ (integrated as $\beta * \sqrt{dt}$).

Simulations were obtained using the Euler method for numerical integration with a time step $dt$ = $10^{-3}$ seconds.

## Acknowledgments

Portuguese Foundation for Science and Technology (FCT) grant UIDB/50026/2020 (JC)
Portuguese Foundation for Science and Technology (FCT) grant UIDP/50026/2020 (JC)
Portuguese Foundation for Science and Technology (FCT) grant CEECIND/03325/2017 (JC)
European Research Council (ERC) grant 679058 (NS, FFF)
Portuguese Foundation for Science and Technology (FCT) grant 275-FCT-PTDC/BBB/IMG/5132/2014 (NS, FFF)
Lisboa Regional Operational Programme (Lisboa 2020), under the PORTUGAL 2020 Partnership Agreement through the European Regional Development Fund (ERDF)
Portuguese Foundation for Science and Technology (FCT) grant LISBOA-01-0145-FEDER-022170.

## Author contributions

Conceptualization: JC, NS

Methodology: JC, NS, FFF

Investigation: JC, FFF, NS

Visualization: JC

Funding acquisition: JC, NS

Project administration: NS

Supervision: JC, NS

Writing – original draft: JC, NS

Writing – review & editing: JC, NS, FFF

bioRxiv preprint doi: https://doi.org/10.1101/2022.01.06.475200; this version posted January 6, 2022. The copyright holder for this preprint (which was not certified by peer review) is the author/funder, who has granted bioRxiv a license to display the preprint in perpetuity. It is made available under aCC-BY-NC-ND 4.0 International license.

## Competing interests:

Authors declare that they have no competing interests.

## Data and materials availability:

All MRI data, code and materials used in this study are available in https://drive.google.com/drive/folders/1s99k5H1riQV-QONHrn-6cEphbv2VctLv?usp=sharing, which will be deposited in a public database upon acceptance.

Further details on data and materials are provided in Supplementary Material.

bioRxiv preprint doi: https://doi.org/10.1101/2022.01.06.475200; this version posted January 6, 2022. The copyright holder for this preprint (which was not certified by peer review) is the author/funder, who has granted bioRxiv a license to display the preprint in perpetuity. It is made available under aCC-BY-NC-ND 4.0 International license.

# References


1. M. D. Fox, M. E. Raichle, Spontaneous fluctuations in brain activity observed with functional magnetic resonance imaging. *Nature reviews neuroscience* **8**, 700-711 (2007).
2. B. B. Biswal *et al.*, Toward discovery science of human brain function. *Proceedings of the National Academy of Sciences of the United States of America* **107**, 4734-4739 (2010).
3. C. J. Stam, Modern network science of neurological disorders. *Nature reviews. Neuroscience* **15**, 683-695 (2014).
4. A. Fornito, A. Zalesky, M. Breakspear, The connectomics of brain disorders. *Nature reviews. Neuroscience* **16**, 159-172 (2015).
5. J. E. Chen *et al.*, Resting-state "physiological networks". *NeuroImage* **213**, 116707 (2020).
6. M. Breakspear, Dynamic models of large-scale brain activity. *Nature neuroscience* **20**, 340-352 (2017).
7. O. Sporns, Contributions and challenges for network models in cognitive neuroscience. *Nature neuroscience* **17**, 652 (2014).
8. J. Cabral, M. Kringelbach, G. Deco, Functional Connectivity dynamically evolves on multiple time-scales over a static Structural Connectome: Models and Mechanisms. *NeuroImage* **160**, 84-96 (2017).
9. L. Coletta *et al.*, Network structure of the mouse brain connectome with voxel resolution. *Science Advances* **6**, eabb7187 (2020).
10. S. M. Smith *et al.*, Correspondence of the brain's functional architecture during activation and rest. *Proceedings of the national academy of sciences* **106**, 13040-13045 (2009).
11. J. S. Damoiseaux *et al.*, Consistent resting-state networks across healthy subjects. *Proceedings of the National Academy of Sciences of the United States of America* **103**, 13848-13853 (2006).
12. B. B. Biswal *et al.*, Toward discovery science of human brain function. *Proceedings of the National Academy of Sciences* **107**, 4734-4739 (2010).
13. R. C. Craddock *et al.*, Imaging human connectomes at the macroscale. *Nature methods* **10**, 524-539 (2013).
14. V. D. Calhoun, R. Miller, G. Pearlson, T. Adali, The chronnectome: time-varying connectivity networks as the next frontier in fMRI data discovery. *Neuron* **84**, 262-274 (2014).
15. M. G. Preti, T. A. Bolton, D. Van De Ville, The dynamic functional connectome: State-of-the-art and perspectives. *NeuroImage* **160**, 41-54 (2017).
16. Y. Gu *et al.*, Brain activity fluctuations propagate as waves traversing the cortical hierarchy. *Cerebral cortex* **31**, 3986-4005 (2021).
17. R. V. Raut *et al.*, Global waves synchronize the brain's functional systems with fluctuating arousal. *Science advances* **7**, eabf2709 (2021).
18. N. E. Fultz *et al.*, Coupled electrophysiological, hemodynamic, and cerebrospinal fluid oscillations in human sleep. *Science* **366**, 628-631 (2019).
19. W.-J. Pan, G. J. Thompson, M. E. Magnuson, D. Jaeger, S. Keilholz, Infraslow LFP correlates to resting-state fMRI BOLD signals. *NeuroImage* **74**, 288-297 (2013).
20. G. J. Thompson, W. J. Pan, M. E. Magnuson, D. Jaeger, S. D. Keilholz, Quasi-periodic patterns (QPP): Large-scale dynamics in resting state fMRI that correlate with local infraslow electrical activity. *NeuroImage* **84**, 1018-1031 (2014).

bioRxiv preprint doi: https://doi.org/10.1101/2022.01.06.475200; this version posted January 6, 2022. The copyright holder for this preprint (which was not certified by peer review) is the author/funder, who has granted bioRxiv a license to display the preprint in perpetuity. It is made available under aCC-BY-NC-ND 4.0 International license.


21. B. J. He, A. Z. Snyder, J. M. Zempel, M. D. Smyth, M. E. Raichle, Electrophysiological correlates of the brain's intrinsic large-scale functional architecture. *Proceedings of the National Academy of Sciences of the United States of America* **105**, 16039-16044 (2008).
22. L. D. Lewis, K. Setsompop, B. R. Rosen, J. R. Polimeni, Fast fMRI can detect oscillatory neural activity in humans. *Proceedings of the national academy of sciences* **113**, E6679-E6685 (2016).
23. T. M. van Alst *et al.*, Anesthesia differentially modulates neuronal and vascular contributions to the BOLD signal. *NeuroImage* **195**, 89-103 (2019).
24. J. Paasonen, P. Stenroos, R. A. Salo, V. Kiviniemi, O. Gröhn, Functional connectivity under six anesthesia protocols and the awake condition in rat brain. *NeuroImage* **172**, 9-20 (2018).
25. R. Weber, P. Ramos-Cabrer, D. Wiedermann, N. Van Camp, M. Hoehn, A fully noninvasive and robust experimental protocol for longitudinal fMRI studies in the rat. *NeuroImage* **29**, 1303-1310 (2006).
26. D. Gutierrez-Barragan, M. A. Basson, S. Panzeri, A. Gozzi, Infraslow State Fluctuations Govern Spontaneous fMRI Network Dynamics. *Current Biology* **29**, 2295-+ (2019).
27. F. A. Nasrallah, H.-C. Tay, K.-H. Chuang, Detection of functional connectivity in the resting mouse brain. *NeuroImage* **86**, 417-424 (2014).
28. G. J. Thompson, W.-J. Pan, M. E. Magnuson, D. Jaeger, S. D. Keilholz, Quasi-periodic patterns (QPP): large-scale dynamics in resting state fMRI that correlate with local infraslow electrical activity. *NeuroImage* **84**, 1018-1031 (2014).
29. B. Pradier *et al.*, Combined resting state-fMRI and calcium recordings show stable brain states for task-induced fMRI in mice under combined ISO/MED anesthesia. *NeuroImage* **245**, 118626 (2021).
30. X. J. Wang, Neurophysiological and computational principles of cortical rhythms in cognition. *Physiological reviews* **90**, 1195-1268 (2010).
31. A. K. Engel, P. Fries, W. Singer, Dynamic predictions: oscillations and synchrony in top-down processing. *Nature reviews. Neuroscience* **2**, 704-716 (2001).
32. G. Buzsaki, *Rhythms of the brain*. (Oxford University Press, Oxford, 2006), pp. xiv, 448 p.
33. P. J. Drew, C. Mateo, K. L. Turner, X. Yu, D. Kleinfeld, Ultra-slow oscillations in fMRI and Resting-State connectivity: neuronal and vascular contributions and technical confounds. *Neuron*, (2020).
34. C. F. Beckmann, M. DeLuca, J. T. Devlin, S. M. Smith, Investigations into resting-state connectivity using independent component analysis. *Philosophical transactions of the Royal Society of London. Series B, Biological sciences* **360**, 1001-1013 (2005).
35. M. G. Preti, T. A. Bolton, D. Van De Ville, The dynamic functional connectome: State-of-the-art and perspectives. *NeuroImage*, (2016).
36. R. M. Hutchison *et al.*, Dynamic functional connectivity: promise, issues, and interpretations. *NeuroImage* **80**, 360-378 (2013).
37. J. E. Chen, C. Chang, M. D. Greicius, G. H. Glover, Introducing co-activation pattern metrics to quantify spontaneous brain network dynamics. *NeuroImage* **111**, 476-488 (2015).
38. F. I. Karahanoğlu, D. Van De Ville, Transient brain activity disentangles fMRI resting-state dynamics in terms of spatially and temporally overlapping networks. *Nature communications* **6**, 7751 (2015).
39. E. Tagliazucchi, P. Balenzuela, D. Fraiman, D. R. Chialvo, Criticality in large-scale brain FMRI dynamics unveiled by a novel point process analysis. *Frontiers in physiology* **3**, 15 (2012).

bioRxiv preprint doi: https://doi.org/10.1101/2022.01.06.475200; this version posted January 6, 2022. The copyright holder for this preprint (which was not certified by peer review) is the author/funder, who has granted bioRxiv a license to display the preprint in perpetuity. It is made available under aCC-BY-NC-ND 4.0 International license.


40. J. Cabral, E. Hugues, O. Sporns, G. Deco, Role of local network oscillations in resting-state functional connectivity. *NeuroImage* **57**, 130-139 (2011).
41. A. Ponce-Alvarez *et al.*, Resting-state temporal synchronization networks emerge from connectivity topology and heterogeneity. *PLoS computational biology* **11**, e1004100 (2015).
42. S. Atasoy, I. Donnelly, J. Pearson, Human brain networks function in connectome-specific harmonic waves. *Nature communications* **7**, 10340 (2016).
43. P. A. Robinson *et al.*, Eigenmodes of brain activity: Neural field theory predictions and comparison with experiment. *NeuroImage* **142**, 79-98 (2016).
44. G. Deco *et al.*, Awakening: Predicting external stimulation to force transitions between different brain states. *Proceedings of the National Academy of Sciences* **116**, 18088-18097 (2019).
45. J. Cabral *et al.*, Cognitive performance in healthy older adults relates to spontaneous switching between states of functional connectivity during rest. *Scientific reports* **7**, 5135 (2017).
46. P. Tewarie *et al.*, How do spatially distinct frequency specific MEG networks emerge from one underlying structural connectome? The role of the structural eigenmodes. *NeuroImage*, (2018).
47. K. J. Friston, J. Kahan, A. Razi, K. E. Stephan, O. Sporns, On nodes and modes in resting state fMRI. *NeuroImage* **99**, 533-547 (2014).
48. E. A. Allen *et al.*, Tracking whole-brain connectivity dynamics in the resting state. *Cerebral cortex* **24**, 663-676 (2014).
49. E. C. Hansen, D. Battaglia, A. Spiegler, G. Deco, V. K. Jirsa, Functional connectivity dynamics: modeling the switching behavior of the resting state. *NeuroImage* **105**, 525-535 (2015).
50. A. B. A. Stevner *et al.*, Discovery of key whole-brain transitions and dynamics during human wakefulness and non-REM sleep. *Nature communications* **10**, 1035 (2019).
51. V. K. Jirsa, H. Haken, Field theory of electromagnetic brain activity. *Physical review letters* **77**, 960 (1996).
52. P. L. Nunez, The brain wave equation: a model for the EEG. *Mathematical Biosciences* **21**, 279-297 (1974).
53. G. Deco, V. K. Jirsa, P. A. Robinson, M. Breakspear, K. Friston, The dynamic brain: from spiking neurons to neural masses and cortical fields. *PLoS computational biology* **4**, e1000092 (2008).
54. H. S. Samanta, J. K. Bhattacharjee, A. Bhattacharyay, S. Chakraborty, On noise induced poincaré–andronov–Hopf bifurcation. *Chaos: An Interdisciplinary Journal of Nonlinear Science* **24**, 043122 (2014).
55. I. U. A. Kuznetsov, *Elements of applied bifurcation theory*. Applied mathematical sciences (Springer, New York, ed. 2nd, 1998), pp. xix, 591 p.
56. G. Deco *et al.*, Single or multiple frequency generators in on-going brain activity: A mechanistic whole-brain model of empirical MEG data. *NeuroImage* **152**, 538-550 (2017).
57. G. Deco, M. Kringelbach, Metastability and Coherence: Extending the Communication through Coherence Hypothesis Using a Whole-Brain Computational Perspective. *Trends in neurosciences* **39**, 432 (2016).
58. J. Cabral *et al.*, Cognitive performance in healthy older adults relates to spontaneous switching between states of functional connectivity during rest. *Scientific reports* **7**, (2017).

bioRxiv preprint doi: https://doi.org/10.1101/2022.01.06.475200; this version posted January 6, 2022. The copyright holder for this preprint (which was not certified by peer review) is the author/funder, who has granted bioRxiv a license to display the preprint in perpetuity. It is made available under aCC-BY-NC-ND 4.0 International license.

59. J. Vohryzek, G. Deco, B. Cessac, M. L. Kringelbach, J. Cabral, Ghost Attractors in Spontaneous Brain Activity: Recurrent Excursions Into Functionally-Relevant BOLD Phase-Locking States. *Frontiers in systems neuroscience* **14**, (2020).
60. L. D. Lord *et al.*, Dynamical exploration of the repertoire of brain networks at rest is modulated by psilocybin. *NeuroImage* **199**, 127-142 (2019).
61. G. Paxinos, C. Watson, *The rat brain in stereotaxic coordinates-The New Coronal Set*. (Elsevier, 2004).